Journal of Electroanalytical Chemistry 860 (2020) 113889

Contents lists available at ScienceDirect

Journal of Electroanalytical Chemistry

journal homepage: www.elsevier.com/locate/jelechem

Electrodeposition of superconducting rhenium-cobalt alloys from water-in-salt electrolytes

S. De [a], W.D. Sides [a], T. Brusuelas [a], Q. Huang [a,b,*]

[a] Department of Chemical and Biological Engineering, University of Alabama, Tuscaloosa, 35487, United States of America
[b] Alabama Water Institute, University of Alabama, Tuscaloosa, 35487, United States of America

ARTICLE INFO

Article history:
Received 11 May 2019
Received in revised form 21 January 2020
Accepted 23 January 2020
Available online 24 January 2020

Keywords:
Rhenium cobalt alloys
Water-in-salt
Electrodeposition
Superconductor

ABSTRACT

Electrodeposition of rhenium-cobalt (Re-Co) alloys is investigated in water-in-salt electrolyte with a superhigh concentration of lithium chloride. Cyclic and linear sweep voltammetries, potentiostatic deposition, and X-ray fluorescence spectroscopy are used to characterize the electrochemical deposition behavior of electrolytes and determine the deposition rates of each elements. Re deposition rate is enhanced in the presence of Co and a constant alloy composition is observed within a wide range of potential, both of which are explained with a partial ionic stabilization effect of Co on Re. A substitutional solid solution with hexagonal close pack structure is observed for ReCo alloys after annealing, where the lattice parameters linearly scale with the alloy compositions. The effect of Co alloying on the superconductivity of electrodeposited alloy films is also characterized down to 2 K.

1. Introduction

Electrodeposited superconducting materials can be used to fabricate superconducting circuits for cryogenic quantum devices. A superconducting critical temperature (T_c) of about 6 K was recently reported for electrodeposited rhenium [1], which represents a significant increase from its bulk material, 1.7 K [2,3]. However, a formation of rhenium oxide intermediate typically occurs during the electrodeposition, which prevents the further reduction into rhenium metal [4] and mandates the use of highly acidic electrolyte for rhenium electrodeposition [1,5–7]. The significant amount of proton in the electrolyte often results in not only hydrogen incorporation and low current efficiency but also cracks in the highly stressed films deposited thereof.

Water-in-salt is an aqueous electrolyte with super high concentration of salt, where the hydration of salt depletes or significantly lowers the concentration of free water molecules. This depletion of water suppresses the reduction of proton and water, and widens the electrochemical window of electrolyte [8,9]. Such behaviors were recently utilized to enable the lithiation–delithiation process or improve coulombic efficiencies in various aqueous battery systems [8,10–12].

On the other hand, water-in-salt electrolyte can be of interest to electrodeposition as well, particularly for less noble metals, which are deposited at potentials more negative than hydrogen evolution reaction or water reduction. While non-aqueous approaches, such as organic solvents, molten salts, and ionic liquids have been investigated for the same purpose, the water-in-salt electrolytes provide an alternative approach with high solubility of inorganic salts, low cost, low toxicity and ease of operation. A water-in-salt electrolyte with superhigh concentration of LiCl has been recently applied to electrodeposit rhenium [13,14], where an increased T_c of 6 K with was also observed. The use of acidic water-in-salt electrolyte significantly suppressed the hydrogen evolution and completely eliminated the film cracks [13]. A hindered degradation of T_c upon thermal annealing was observed for the films deposited thereof, hence an improved stability of superconductivity [14]. In addition, the suppression of hydrogen evolution reaction significantly decreases the solution resistance effect and enables the electrochemical study of the deposition behavior at more negative potentials.

Films with a further increased T_c and a further improved thermal stability are sought after for the fabrication of circuits. One of the approaches is to investigate the alloying of Re with other elements. However, electrodeposition of superconducting Re alloys have not been reported to our best knowledge. Furthermore, while the mainstream cryogenic quantum devices have been based on the superconductor-insulator-superconductor Josephson junctions, more recent studies on the so-called π-phase Josephson junction showed that superconductor-ferromagnet-superconductor sandwich structures provide additional control of the quantized junction current through an external magnetic field [15–17]. Pulsed electrodeposition of alloy layers with different compositions provides a path to fabricate such junctions from a single process, if both ferromagnetic and superconducting alloys can be deposited from a single electrolyte. How the incorporation of a magnetic

* Corresponding author at: Department of Chemical and Biological Engineering, University of Alabama, Tuscaloosa, 35487, United States of America.
E-mail address: qhuang@eng.ua.edu. (Q. Huang).

http://dx.doi.org/10.1016/j.jelechem.2020.113889

element impacts the superconductivity of electrodeposited superconductor needs to be understood. This paper reports a study on the electrodeposition of superconducting ReCo alloys from acidic water-in-salt electrolytes, where the superconducting Re is co-deposited with a magnetic element, Co. The effect of super high concentration of LiCl on the electrodeposition of elemental Co and Re is also studied for comparison. The synergistic interaction between Re and Co during electrodeposition is discussed. In addition, the impacts of Co alloying on the film morphology, crystallographic structure and superconductivity of electrodeposited alloy films are presented as well.

2. Experimental

2.1. Electrochemical cell

A three-electrode cell with a glass frit to separate the catholyte and anolyte is used for the studies. A 99.99% platinum foil in the anolyte compartment is used as the anode. A saturated calomel electrode (SCE) is used as a reference electrode and the reference compartment is attached to catholyte compartment via a capillary tube. All potentials are referred to with respect to this SCE. Rotating disk electrodes (RDE) with a diameter of 5 mm, or a surface area of 0.2 cm^2, are used as the cathode. Platinum RDE is used for electrochemical studies such as cyclic voltammetry and anodic stripping. Copper RDEs are used to electrodeposit ReCo films at constant potentials to characterize alloy compositions and determine partial deposition currents.

2.2. Materials and chemicals

Si coupons with Au strip patterns are used to deposit ReCo films for superconductivity measurements. Si wafers with a layer of 50 nm thermal SiO_2 are used as the substrate to fabricate Au strips. UV lithography is used to define the pattern in photoresist. 10 nm Ti and 100 nm Au are consecutively evaporated without air gap on the patterned wafer. The strip patterns are finally created by lifting off the photoresist. The strips are 1 mm wide and 10 mm long, connecting with a 3 mm wide and 5 mm long pad, with the total plating surface area similar to RDE of 0.2 cm^2. Fresh solution is used for every batch of experiments and the total amount of materials deposited from one batch of experiments is negligible compared with the amount of metals present in the electrolyte. The total volume of the electrolyte is therefore not controlled, but between 50 and 100 mL. The Si coupon is mounted on a holder rotating in the same way as RDE. Electrical connections are made through a front contact to the pad.

Different substrate materials, Pt, Cu and Au, are used for the electrochemical studies and the superconductivity samples preparation, where underpotential deposition may occur depending on the work functions of the substrate materials and deposited alloys. However, such substrate effect is believed to be mitigated once a coalescent film of deposit is formed. While poor nucleation density on semiconductor substrates can delay the film coalescence, such effect is often limited up to a few monolayers of deposit on metal substrates. Furthermore, potentiostatic DC deposition is used to prepare film samples for composition, thickness, morphology and superconductivity characterizations. Side reaction may dominate before a mass transport limitation is established in galvanostatic deposition, diminishing the metal deposition. Contrarily, metal deposition can be forced to occur under potentiostatic control regardless of side reaction, further limiting the effect of the substrate.

The deposition solutions contain 0.1 M sulfuric acid (H_2SO_4), 5 M lithium chloride (LiCl), and various amounts of cobalt sulfate ($CoSO_4$) and ammonia perrhenate (NH_4ReO_4). While both sulfate and chloride anions have been reported to adsorb on metal surface, the sulfate adsorbate is often disrupted and displaced by chloride [18]. Furthermore, the adsorbate layers are often disrupted at more negative potential bias [19]. Therefore, the effect of sulfate is believed to be negligible in the presence of a much higher concentration of chloride for the overpotential deposition in this study. The solution pH measured with a pH meter is typically obscured because of the interference from the high concentration of Li^+. In addition, the depletion of free water molecule in water-in-salt electrolytes also changes the concentration product of $[H^+][OH^-]$, which otherwise stays constant at 10^{-14} in dilute solutions. Therefore, the term of pH is not used in this study and proton concentration or hydroxide concentration is used instead. All chemicals are at least ACS grade and deionized water with a resistivity of 18 MΩ-cm is used in all experiments. All experiments are carried out in ambient condition at room temperature, 20 °C.

2.3. Instruments and procedures

Cyclic voltammetry and anodic stripping experiments are carried out to characterize the electrochemical behavior of various electrolytes. A scan rate of 20 mV/s is used for all voltammetry studies. Electrochemical impedance is acquired with a 10-mV sinusoidal potential perturbation to determine the solution resistance and correct the voltage drop in solution. All the electrolytes show a very similar resistance, between 8 and 9 Ω, due to the dominant effect of high concentration of LiCl and H_2SO_4. The deposition areas are kept almost the same between RDEs and Au strips so the solution resistance effect will also be the same during potentiostatic deposition. Therefore, direct comparison between results in this paper can be conducted while all the potentials are reported without the ohmic drop correction.

An Autolab 302N potentiostat with frequency analyzer is used for all electrochemical studies. A Bruker M1 Mistral X-ray fluorescence (XRF) with a 0.7 mm collimator and 50 kV is used to determine the composition and thickness of electrodeposited films. The composition and thickness are averaged from five points along the diameter of a single copper RDE. The weight percent compositions obtained from XRF are converted into atomic percent, assuming the elements are present as metal. No metal elements other than Re, Co and the substrate were detected. The XRF instrument is not capable of quantifying light elements. The impurity elements incorporated during electrodeposition have been studied separately for pure Re films deposited from a similar electrolyte using secondary ion mass spectroscopy [20]. Chlorine and oxygen are the two most abundant impurities, but both well below 1%. Furthermore, no negative effects were observed for impurity incorporation on the superconductivity of Re films. A JEOL-7000 field emission scanning electron microscope (SEM) is used to characterize the morphology of film. A home built vacuum annealing chamber is used to anneal the films at a pressure below 1E − 4 Torr. Crystallographic analysis is carried out using a Bruker D8 power X-ray diffractometer (XRD) with Co Kalpha source (wavelength = 1.79 Å), operated at 40 kV and 40 mA. The specimen is fixed on a horizontal sample stage and a standard scanning with no specimen tilting or rotation is applied. A Quantum Design Dynacool Physical Property Measurement System (PPMS) is used to measure the film resistance on the strips down to 2 K and determine the superconducting critical temperature. A sputtering coater is used to deposit a 30-nm thick Au capping layer on the electrodeposited Re or ReCo strips to prevent oxidation and contamination in the ambient, as well as to ease the wire bonding. Aluminum wires are bonded between the Au capped strip and the puck to form the four-probe configuration. A constant current configuration with 1 mA is used for the resistance measurement.

3. Results and discussion

3.1. Proton reduction reaction

Linear sweep voltammetry is acquired first on Pt RDE in electrolytes with LiCl and H_2SO_4 only. A high rotation speed of 1600 rpm is used to prevent surface blockage by hydrogen bubbles. Fig. 1(a) shows the comparison between three solutions with 3, 5 and 8 M LiCl, all containing 0.1 M H_2SO_4. A limiting current is observed for proton reduction and it decreases from 283 mA/cm^2 for 3 M LiCl to 201 and 129 mA/cm^2, or by 30% and 54%, for 5 and 8 M LiCl, respectively. The high ionic strength of the electrolyte is also expected to cause ionic behavior different from dilute solutions. While a detailed calculation was published earlier [14], the activity

coefficient of proton approximated using Debye-Hückel theory decreases from 0.55 in 3 M LiCl to 0.53 and 0.51 for 5 and 8 M LiCl, respectively. This is expected to result in respectively 4% and 7% decrease in the limiting current. While the total amount of water only decreases slightly among these three solutions, the amount of free water molecules or the water molecules that behave in the same way as pure water are significantly depleted as the concentration of LiCl increases. Fig. 1(b) shows the photographs of two Co electrolytes with 5 M and 6 M LiCl, respectively, both containing 0.1 M H_2SO_4 and 0.01 M $CoSO_4$. It is well known that hydrated Co^{2+} exhibits pink color while the anhydrous Co^{2+} is blue. The two photos therein clearly demonstrate that free water molecules are almost completely depleted at a LiCl concentration around 5 and 6 M. It takes 4 and 6 water molecules to fully hydrate a Li^+ cation and a Cl^-, respectively, in an infinitely diluted solution [21]. This results in a consumption of 10 H_2O molecules for each pair of Li^+Cl^-, had LiCl been fully hydrated. On the other hand, 48 mole water is needed to prepare 1 L of 5 M LiCl electrolyte, barely enough to fully hydrate all the ions. While ionic paring and ionic penetration into the inner water sheath can occur [22,23], relaxing the number of water molecules needed, the water molecules in electrolytes with 5 to 6 M LiCl behave completely different from dilute electrolytes. This also results in a complete disruption of hydrogen bond network among free water molecules and significantly decreases the proton diffusion, consistent with the decrease of the limiting current observed in Fig. 1(a).

3.2. Elemental electrodeposition

Fig. 2(a) shows the cyclic voltammograms acquired on Pt RDE in an electrolyte with 5 M LiCl, 0.1 M H_2SO_4 and 0.01 M $CoSO_4$. Two rotation speeds of 400 and 1600 rpm are used for comparison. First, a hysteresis is observed between -0.25 and -0.75 V, due to a surface change from Pt to Co. Proton reduction is much more facilitated on Pt surface than on Co, reaching the limiting current density of about -100 mA/cm^2 at

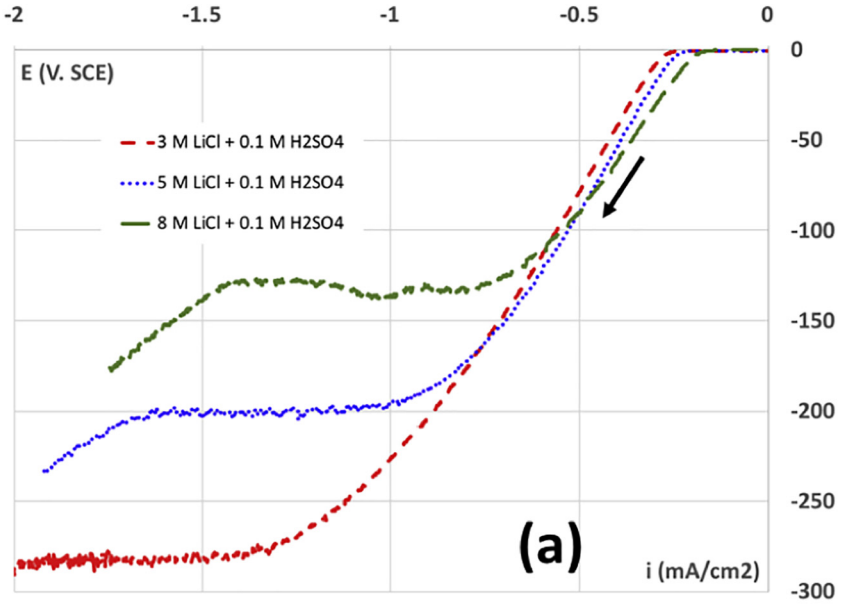

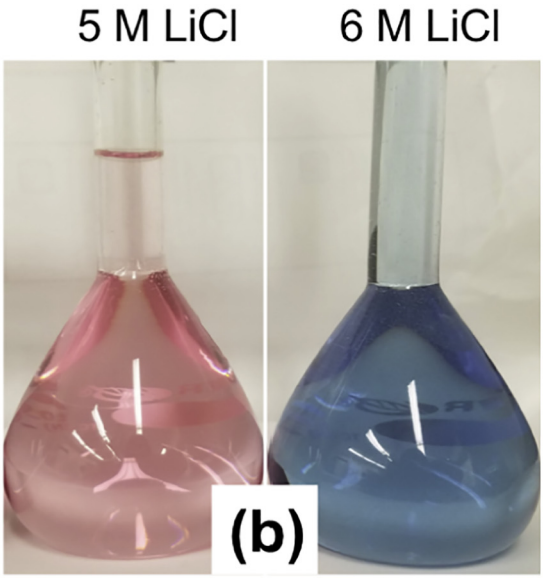

Fig. 1. (a) Linear sweep voltammograms acquired on Pt RDE at 1600 rpm from electrolytes containing 0.1 M H_2SO_4 with 3, 5 and 8 M LiCl; (b) photographs of Co electrolytes containing 0.01 M $CoSO_4$, 0.1 M H_2SO_4 with 5 and 6 M LiCl. The voltage sweep rate is 20 mV/s.

400 rpm at about −0.6 V. As the potential continues to decrease, Co deposition starts at about −0.75 V, gradually converting the Pt surface into Co surface. The current starts to decrease along with the Co deposition because of a much slower reaction kinetics of proton reduction on Co. The current plateau recovers at −1.1 V once the limiting current is reached again on Co surface. As the rotation speed is increased to 1600 rpm, the limiting current density doubles but is not reached on Pt electrode before Co deposition starts. This results in a peak current at −0.9 V as the Pt electrode is partially covered by Co, a current dip at −1.1 V as the Pt is completely covered by Co, and a limiting current density on Co electrode at −1.4 V.

Potentiostatic deposition is carried out on Cu RDEs to determine the Co deposition rates. Film thickness is determined using XRF and the Co deposition partial current densities calculated with Faraday's law at different potentials are also presented in Fig. 2(a). Co deposition partial current starts at about −0.75 V, consistent with the current dip observed in CV. It reaches a limiting current plateau at −1 V and stays relative constant before it significantly drops at −1.5 V, where Co deposition almost completely ceased.

The mass transport limiting current for Co deposition at 400 rpm in Fig. 2(a) is determined to be −2.68 mA/cm^2. A separate study on copper deposition from the same 5 M LiCl water-in-salt electrolyte has been carried out [24]. Due to the nobleness of copper, the diffusion coefficient and activity coefficient of Cu^{2+} was easily determined to be 5.94E−6 cm^2/s and 0.562, respectively, using electrochemical analytical techniques. Similar coefficients are expected for Co^{2+} due to the similar ionic sizes and charge between the two. A limiting current of −2.7 mA/cm^2 would be expected with the same coefficients, which agrees with the experimental observation extremely well.

The decrease of Co deposition rate at highly negative potentials seems to coincide with the water reduction reaction. A very recent study on the electrochemistry of Li^+ and Na^+ cations in organic solvents with a small amount of water reported a decreased water reduction rate at highly

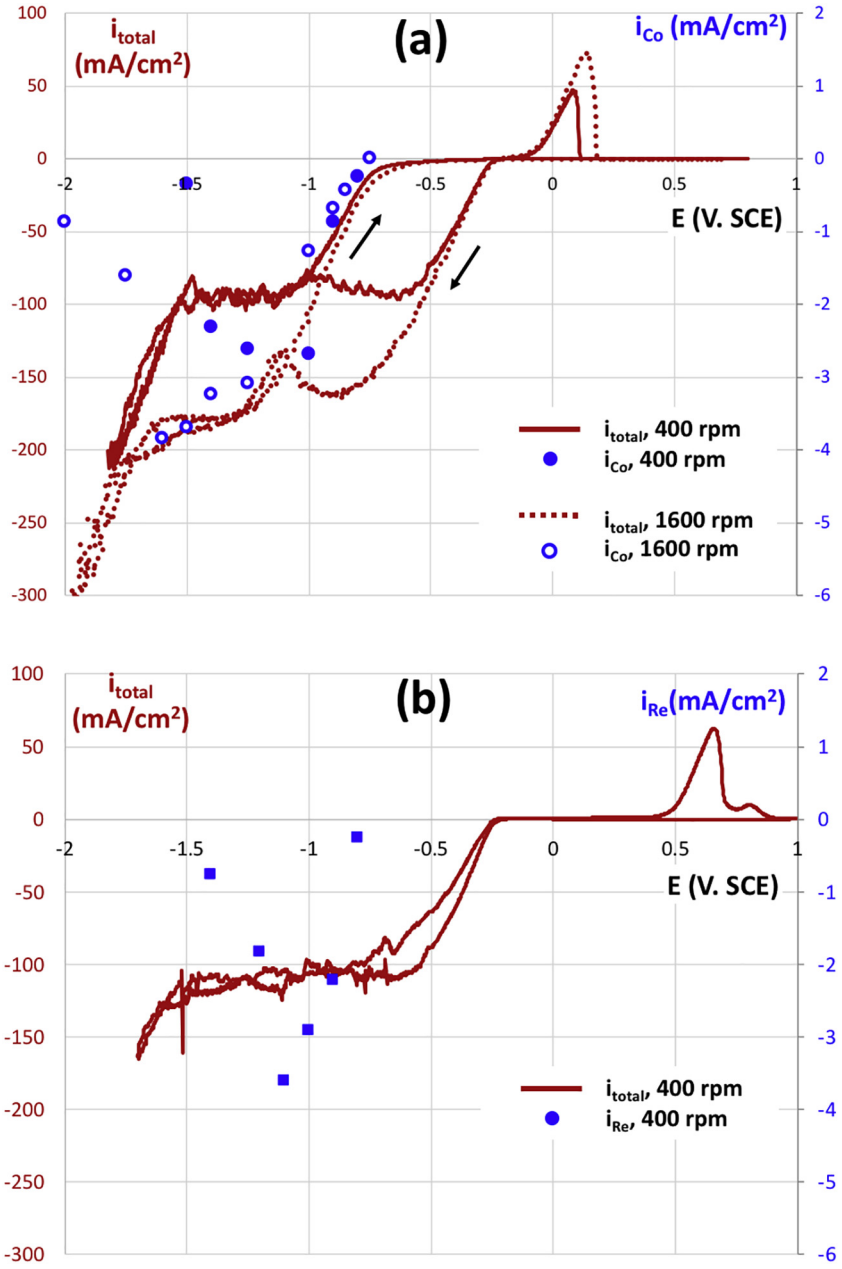

Fig. 2. (Crimson) Cyclic voltammograms and (blue) partial deposition current densities acquired on RDE (a) at 400 and 1600 rpm from Co electrolyte containing 0.01 M $CoSO_4$; and (b) at 400 rpm from Re electrolyte containing 0.025 M NH_4ReO_4. All electrolytes contained 0.1 M H_2SO_4 and 5 M LiCl. The voltage sweep rate is 20 mV/s. (For interpretation of the references to color in this figure legend, the reader is referred to the web version of this article.)

negative potential in the presence of Li^+ (but not Na^+) [25]. The formation of LiOH upon water reduction and its low solubility, but not NaOH, was proposed to passivate the electrode surface and suppress the water reduction. Water-in-salt electrolytes with the free water molecules depleted are expected to behave alike. The suppressed Co deposition observed upon water reduction in this study is believed to relate to the same electrode passivation by LiOH. Furthermore, Co deposition typically involves two consecutive steps through an intermediate adsorbed on electrode surface [26–28] such as $CoOH^+_{ads}$. The formation and competitive adsorption of LiOH, even not fully passivating the electrode, is expected to suppress the Co deposition. While the surface proton concentration is expected to drop significantly between −1 and −1.4 V as the proton reduction limiting current is reached, little suppression on Co deposition is observed. A quick numerical simulation of the one-dimensional proton mass transport on RDE is carried out to fit the proton reduction current on cobalt (see Fig. S1 in Supplementary materials). The surface proton concentration is estimated to be between 10^{-3} to 10^{-7} mol/L between −1 to −1.4 V with the fitted parameters. LiOH is expected to remain more soluble at these mild acidic conditions. Only after the water reduction starts does the surface hydroxide concentration reach a much higher value and the LiOH blockage occurs.

The elemental deposition of Re is studied in a similar way using an electrolyte containing 5 M LiCl, 0.1 M H_2SO_4 and 0.025 M NH_4ReO_4. A more detailed discussion has been published elsewhere [13], but an example CV with the partial current density at 400 rpm is presented in Fig. 2 (b) for a brief comparison. The hysteresis observed in Co case is eliminated because the proton reduction activity on Re is close to Pt, much higher than Co [29]. Re deposition starts at a potential of about −0.8 V, which is similar to Co deposition. On the other hand, the anodic stripping peak starts at 0.4 V, much more positive than the stripping of Co. While a similar decrease in deposition rate is also observed at a more negative potential, it occurred at −1.1 V, a much more positive potential than Co and also more positive than the water reduction reaction. The Re deposition current density reaches a maximum of -3.6 mA/cm^2 before it decreases. A further reduction of Re metal into rhenide anion (Re^-) at a more negative potential, either as a free anion or as a solubable complex with other ionic species, is believed to be involved in this rate decrease.

3.3. ReCo alloy electrodeposition

The electrodeposition of ReCo alloys is first studied using electrolyte containing both 0.01 M $CoSO_4$ and 0.025 M NH_4ReO_4. The electrolyte also contains 5 M LiCl and 0.1 M H_2SO_4 to allow direct comparison with the elemental deposition studies. Cyclic voltammetry is first acquired on Pt RDE. As shown in Fig. 3(a), the majority of anodic stripping starts at 0.3 V, slightly less positive than pure Re but much more positive than pure Co. A much smaller stripping peak starting at 0 V precedes the major anodic stripping, suggesting the presence of two phases with different nobility. While it is not clear from CV whether one or both of them are elemental metals or binary alloys, the total stripping charge is significantly greater than the sum of the elemental Co and Re cases, suggesting a synergistic interaction between the two elements during electrodeposition. A direct comparison is presented in Fig. S2 in Supplementary materials, where the CVs of three cases are overlaid.

DC deposition studies at different constant potentials are carried out on copper RDE and the partial deposition current densities are calculated from the film thickness and alloy composition. Deposition starts at about −0.8 V, similar to the pure elemental deposition cases. A mass transport limited maximum current density of Co is reached at −1.1 V, similar to the elemental deposition of Co. A maximum Re deposition rate is also observed at −1.1 V, also similar to the elemental deposition of Re. But the magnitude of this maximum current density has drastically increased from the latter, from −3.6 to −12.8 mA/cm^2. More importantly the Re deposition rate at more negative potential decreases in a much slower rate in alloy deposition than in elemental Re deposition, suggesting not only a promotion on the Re deposition at less negative potentials but also an inhibition on the reduction of Re metal to rhenide at more negative potentials. Rhenium alloy deposition with iron-group metals at an elevated temperature from conventional aqueous electrolytes with a complexing agent such as citrate has been studied [30–32], where a faster Re deposition rate was also reported in galvanostatic deposition. A catalytic mechanism was proposed, where Re is electroless deposited upon the oxidation of electrodeposited iron group metal [31], or a displacement reaction. While the water-in-salt electrolyte in this study does not contain citrate, a similar electroless catalytic mechanism may still occur. However, a high turnover is necessary to account for the much higher Re content than Co in the alloy deposits. Further discussion will be provided on this catalytical mechanism in Fig. 3(b). On the other hand, the promoted Re deposition rate and suppressed further reduction may also relate to the formation of a thermodynamically more stable CoRe bimetallic phase. While no stoichiometrically well-defined compounds have been reported between Co and Re [33], partial charge transfer can occur between two elements due to the difference in electronegativity or work function. Such partial charge transfer is expected to facilitate the deposition of Re, so called underpotential co-deposition [34,35], and to stabilize the Re atoms from being further reduced. Another type of mechanism of the increase in Re deposition rate at higher potential can involve a chemical formation and precipitation of CoRe bimetallic compound between the Re^- anion and the Co^{2+} cation in the solution. However, it is not clear here if the Gibbs energy of formation of such alloy is sufficient to drive the chemical reaction.

Another alloy electrolyte with the same constituents and concentrations except for a 10-time lower $CoSO_4$ concentration of 0.001 M is also studied and the results are presented in Fig. 3(b). First, the deposition rate of Co still follows a similar trend as in Fig. 2(a), where the deposition starts at about −0.8 V and is almost completely inhibited at potential more negative than −1.4 V. A much lower current plateau is also observed, approximately 10 times lower than in Fig. 3(a), representing the mass transport limit of Co deposition. At the same time, a plateau at about −2.5 mA/cm^2 is observed for the Re partial current density. This current plateau is much lower than the Re deposition rate in Fig. 3(a) despite a same ReO_4^- concentration in electrolyte. This is however similar to the Re deposition current in elemental Re electrolyte and is believed to be consistent with the much lower $CoSO_4$ concentration. This extremely low Co^{2+} concentration in electrolyte results in a negligible enhancement of Re deposition at less negative potentials and a weaker inhibition on the further reduction of Re to Re^- at more negative potentials. The negligible effect of small amount of Co on Re deposition rate may suggest that the displacement-based catalysis of Re deposition with a fast turnover, as discussed in Fig. 3(a) and proposed in literature [30–32] for complexed conventional aqueous electrolyte, did not occur in this water-in-salt electrolyte. However, more studies are needed to clarify this. Nevertheless, the deposition rate of Re is highly correlated with the Co deposition.

In spite of the much different deposition rates between the two electrolytes, the anodic sweep shows the same two stripping peaks for both solutions. The first peak starts at about 0 V and the second one starts at 0.3 V. The stripping of elemental Co starts from a more negative potential of −0.2 V (Fig. 2(a)). Furthermore, the total charge integrated under the first stripping peak in Fig. 3(a) is even higher than the total charge expected from the Co deposition partial current. This further suggests that the first peak results from the anodic stripping of a CoRe binary alloy rather than pure Co. The height of this first peak slightly decreases from 7.4 mA/cm^2 to 6.0 mA/cm^2 when the $CoSO_4$ concentration decreases for 10 times, suggesting the amount of this type of alloy only slightly decreased when the $CoSO_4$ concentration decreases. On contrary, the height of second peak decreases by 4.4 times from 124 to 28 mA/cm^2, consistent with the significant decrease of rhenium deposition rate upon the decrease of Co concentration.

Tables 1 and 2 summarize the compositions of CoRe films deposited at different potentials from the two alloy electrolytes, respectively. It is interesting that all the films deposited between −0.8 and −1.5 V from the first electrolyte with 0.01 $CoSO_4$ fall into a narrow composition

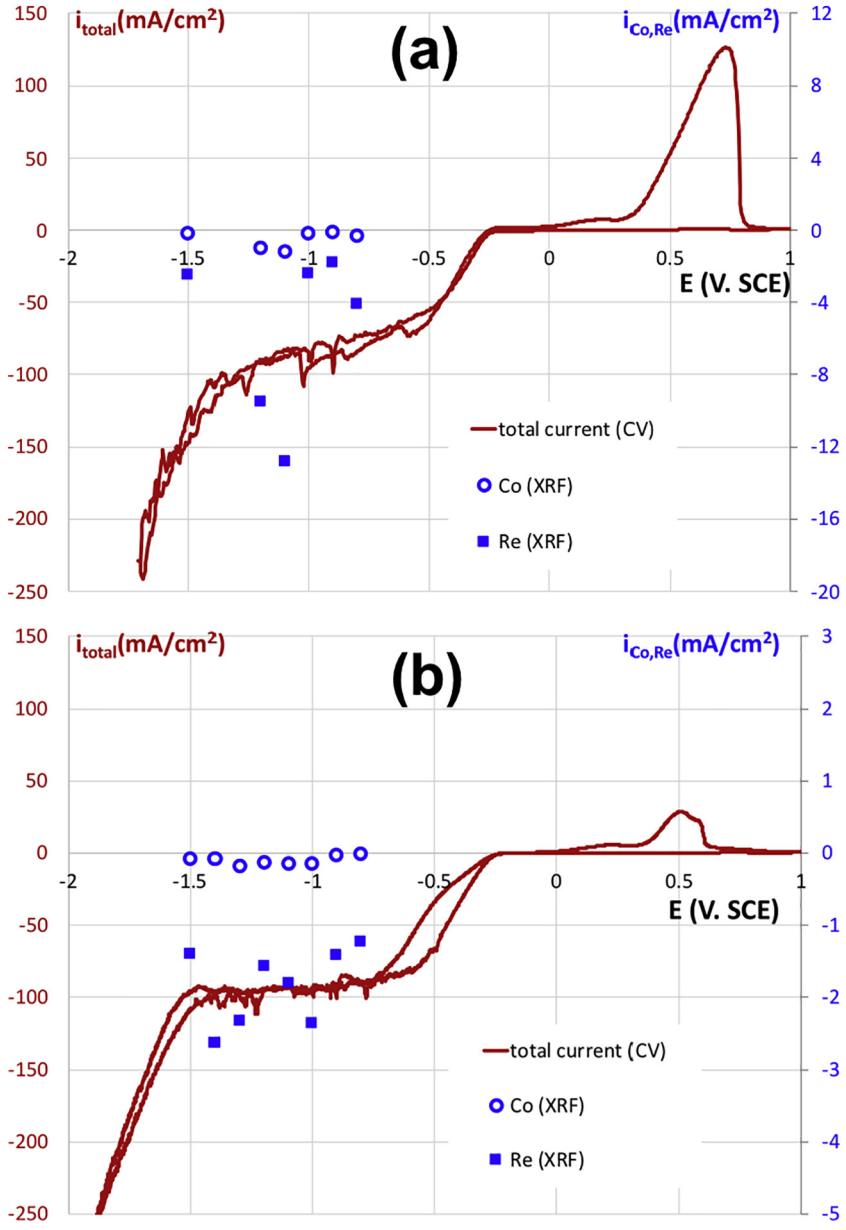

Fig. 3. (Crimson) Cyclic voltammograms and (blue) partial current densities of (solid square) Re and (empty circle) Co deposition acquired on RDE at 400 rpm from the ReCo alloy electrolytes containing 0.025 NH_4ReO_4, 0.1 M H_2SO_4, 5 M LiCl and (a) 0.01 M and (b) 0.001 M $CoSO_4$. The voltage sweep rate is 20 mV/s. (For interpretation of the references to color in this figure legend, the reader is referred to the web version of this article.)

range, from 20 at.% to 27 at.% Co. It is known that elemental deposition of Re alone would have ceased at potential below −1.1 V. If the Co-Re alloy formed mainly through a reaction between Co^{2+} cation and Re^{-} anion, a 1:2 atomic ratio or 66 at.% Re would have been expected. The higher Re contents observed here suggest that Re co-deposited with Co is "protected" from the further reduction into rhenide and each Co atom can stabilize more than two surrounding Re atoms. Even more interestingly, all the films deposited between −1.1 and −1.3 V from the second electrolyte (with much lower Co^{2+} concentration) also falls between 22 and 23 at.% Co. Because of an average 1:3 atomic ratio (about 25 at.% Co) for all the alloys deposited in this potential range regardless of the electrolytes used, we estimate that each Co atom stabilizes about three Re atoms in the deposited alloy films from being further reduced. Any excessive Re atoms are believed to be cathodically stripped. Lower Co contents are observed for films deposited at potentials more positive than −1.1 V and more negative than −1.3 V because of the elemental deposition of Re and inhibition

Table 1
Compositions of alloys electrodeposited at different potentials from alloy electrolyte with 0.01 M $CoSO_4$.

0.01 M Co, 0.025 M Re		
E (V, SCE)	Co at.%	Re at.%
−0.8	20.6	79.4
−0.9	22.4	77.6
−1	21.9	78.1
−1.1	25.2	74.8
−1.2	27.4	72.6
−1.5	20.3	79.7

Table 2
Compositions of alloys electrodeposited at different potentials from alloy electrolyte with 0.001 M $CoSO_4$.

0.001 M Co, 0.025 M Re		
E (V, SCE)	Co at.%	Re at.%
−0.8	6.3	93.7
−0.9	8.7	91.3
−1	18.2	81.8
−1.1	23.1	76.9
−1.2	23.9	76.1
−1.3	21.7	78.3
−1.4	10.5	89.5
−1.5	16.1	83.9

of Co deposition at a high surface concentration of hydroxide, respectively.

3.4. Alloy film properties

SEM is used to characterize the morphology of films deposited on Cu RDE. A complete comparison of ReCo alloy films deposited at different potentials is available in Fig. S3 in Supplementary materials. Nodules of submicron size are observed for all films deposited from −0.8 to −1.1 V. Some directional organization of the nodules is inevitably observed due to the polishing grooves on the RDEs. However, cauliflower shaped features of micron size comprising smaller granules are observed for the films deposited at more negative potentials of −1.2 and −1.5 V. As disused in CV studies in Figs. 2 and 3, a limiting current of Co deposition is reached at −1.1 V, which may have contributed to the formation of cauliflower shaped grains. In addition, the cathodic stripping of Re at potential more negative than −1.1 V seems to be consistent not only with the decrease of Re content starting at −1.1 V (Table 1) but also the commence of cauliflower morphology. It is known from the CV studies that Re deposition is not controlled by diffusion in this alloy electrolyte. A much higher Re deposition partial current is observed, enhanced by the co-deposition of Co. The cauliflower film morphology is believed to mainly relate to the cathodic stripping of excessive Re at extremely negative potentials. In addition, the chemical formation of CoRe from cobaltous cations and rhenide anions may have also contributed. Such chemical precipitation is often observed in electrodeposition of compounds at high potentials, such as metal chalcogenide, where Se or Te was further reduced into anions [36,37]. While the Re is not chalcogen, the further reduction of Re into an anionic species, Re(-I) is expected to facilitate a similar chemical reaction. The detailed speciation and coordination of rhenide anion have been a subject of debate in the past [38–40] and has not been fully understood. However, the chemical precipitation would occur between Co cation and a Re anion, regardless of the detailed speciation of the latter. Furthermore, cobalt hydroxides formed at a high surface hydroxide concentration at more negative potentials is expected to be incorporated and contribute to the cauliflower type morphology as well. Fig. 4 presents a direct comparison between pure Co, pure Re and ReCo alloy films deposited at a similar potential of −1.1 V. Another alloy film deposited at −0.8 V is also included for comparison. All cases are metallic films with silver or gray luster and are at least about 300 nm thick. No substrate effect or thickness dependence is expected from film morphology at this thickness. Completely different morphology is observed between the films. Extremely smooth and almost featureless films with sporadically distributed small protrusions were observed for pure Re. The small protrusions have been previously correlated with a higher chlorine elemental accumulation [14].

Smooth films with randomly distributed nanometer sized ridges are obtained for pure Co films. The morphology of Co films deposited from conventional aqueous electrolytes with mild acidic pH has been found to depend on the electrolyte chemistry and deposition current densities. For example, the addition of chloride anion has been found to facilitate the growth of flake-alike grains with sharp edges at low current densities [41]. While the electrolyte used in this study contains a high concentration of chloride, such flake-shaped grains were not observed. Preferential adsorption of chloride or halides on certain crystal facets has been widely reported in chemical synthesis of nanostructures, resulting in a preferential growth direction of the metal particles [42]. However, such synthesis processes are typically carried out at more thermodynamically equilibrium conditions. A more energetically biased electrodeposition condition, for example a high current density, was found to mitigate such effects, resulting in much smaller and more spherical grains [43]. While the electrolyte used in this study contains 5 M chloride, the electrolyte is extremely acidic and the potential bias or current density is extremely high, mitigating the effect of chloride and resulting in a smooth nano-sized morphology.

Interestingly, nodular films are observed for ReCo films deposited at similar potentials, which are completely different from the elemental metal films. As shown in the CV studies, the total deposition current densities are similar at the same potentials, dominated by the proton reduction. However, the total deposition rate of Re and Co is much faster than the combination of elemental deposition of the two. Therefore, the different morphology observed here for ReCo alloy films is believed to result from a faster deposition rate of metals. On the other hand, the effects of chloride, pH, and voltage or current density are believed to be insignificant. The exact mechanism for this different morphology is unknown and warrants more detailed study in future.

The crystallographic structure of ReCo films as well as the effects of thermal annealing on the crystallographic structure are characterized with XRD. Fig. 5(a) shows the semi-log XRD patterns of the two metallic alloy films shown in Fig. 4(b) and (c), deposited at −0.8 and −1.1 V, respectively. XRD are acquired again after annealing the films in vacuum at 200 °C for 30 min and are presented in Fig. 5(b). Pure Re films in Fig. 4(a), deposited from elemental Re solution at −1.1 V, are also included in the same charts for comparison. Three strong reflection peaks are observed for the Cu RDE substrate. Only two broad peaks are observed for all three as-deposited films, indicative of an amorphous or nanocrystalline nature of the films. Pure Co film deposited from elemental Co electrolyte at −1.1 V, namely the same film presented in Fig. 4(d), is also characterized with XRD before and after 200 °C annealing for 30 min and the patterns are presented in Fig. 5(c). Different from the nanocrystalline Re and ReCo films, polycrystalline Co films are deposited with distinctive peaks observed. Furthermore, no significant change in XRD patterns, or in grain sizes, is observed upon annealing at 200 °C for 30 min for pure Co. The same behaviors are observed for all the metallic pure Co films deposited between −0.8 and −1.1 V.

While the as deposited pure Re and ReCo alloys are of amorphous or nanocrystalline structures, polycrystalline structures are obtained after annealing, resulting in multiple strong peaks in the spectra for all three films. All the peaks can be assigned to an hexagonal close packed (HCP) crystallographic structure, consistent with the facts that Re and Co are both of HCP structure and that the two are completely miscible with each other [33]. A single HCP crystal structure is observed regardless of the film composition, suggesting the formation of binary substitutional solid solution alloys during annealing. As shown in Fig. 5(b), a shift towards higher 2θ angle is observed from pure Re to ReCo alloy for all the peaks, suggesting a decrease in lattice size. Lattice parameters of Re and Co from literature [44] are used to calculate the peak positions, which match the experimental observations extremely well. On the other hand, lattice parameters of ReCo alloys are obtained by fitting the peaks in the experimental spectra. Table 3 summarizes these lattice parameters, where a linear relationship is clearly observed between the lattice size, in both *a* and *c* axes, and the composition. In other words, as the Co content continues to increase in the substitutional solid

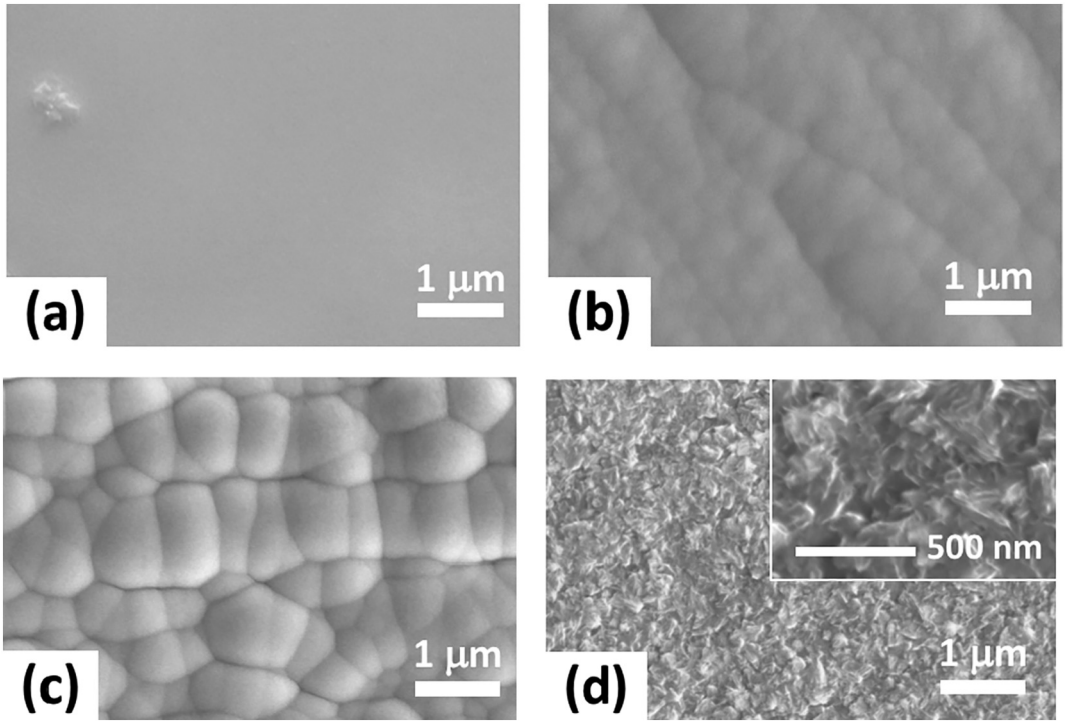

Fig. 4. Top down SEM micrographs of (a) 284 nm pure Re film deposited from Re electrolyte at −1.1 V; (b) 384 nm $Re_{80}Co_{20}$ and (c) 420 nm $Re_{75}Co_{25}$ deposited from ReCo electrolyte at −0.8 V and − 1.1 V, respectively; and (d and inset) 539 nm pure Co deposited from Co electrolyte at −1.1 V. All electrolytes contained 0.1 M H_2SO_4 and 5 M LiCl. Cu RDEs are used as substrate for deposition.

solution, the crystal lattice decreases linearly and isotropically with the increase of the amount of Co atoms.

In addition to the lattice size change, there appears to be a change in preferred crystallographic orientation upon alloying, post annealing. While pure Re shows a preferred growth in *a*-axis, (100) or (200), over *c*-axis, (002), the opposite is observed for $Re_{75}Co_{25}$. This preference is also partially translated to other phases, such as (102), (103), and (110). For example, the former two phases require significant *c*-axis growth are both preferred in $Re_{75}Co_{25}$, while the latter, (110) phase, involves only *a*- and *b*-axis growth and is preferred in pure Re.

The average grain sizes of the films are estimated with Scherrer equation using the full width at half maximum (FWHM) of the (100) or (002) peaks. The broad peaks observed at about 48° are used for the as-deposited films. They are summarized in Table 4. An instrumental broadening of 0.3° is estimated using the Cu(200) peak from the bulk substrate. While the as-deposited films are of an average grain size between 1.6 and 2.7 nm, the grains in annealed films have grown to 100 to 200 nm. A slightly larger grain size may be present for ReCo alloys (in the *c*-axis) than pure Re metals (in the *a*-axis). It is worth mentioning that the absolute values of grain size may be less meaningful as they are averaged across various grains, but the relative comparison between samples is used to here to show the effect of annealing on the grain growth.

Four ReCo alloy films and one pure Re film are electrodeposited on Au strip on silicon substrates to understand the effect of the ferromagnetic element, Co, on the superconductivity of Re films. Superconductivity of the five films, without annealing, are characterized using four-point probe method with temperature being swept from 10 K down to 2 K in PPMS. Such measurements were also attempted with films on Cu RDE but failed due to the thick and conductive RDE substrates. Fig. 6 presents the relationship between sheet resistance and temperature. The sheet resistance is not normalized with thickness and varies across the films. A transition is observed between 5 and 5.8 K for pure Re, below which superconductivity is obtained. This is a significant increase in T_c from the 1.7 K for bulk Re, consistent with our previous observations [14]. Superconductivity is still observed upon the inclusion of 9% Co, with a decreased T_c at 4.6 K. A further increase of Co content to 20% results in a further decrease of T_c to 2.3 K. While an onset of resistance drop is observed at 2.1 K for ReCo film with 23% Co, suggesting a T_c right below 2 K, no such resistance change is observed at all, i.e. no superconductivity is observed beyond 2 K, for ReCo alloy with 25% Co. Bulk Co is a ferromagnetic transition metal. The spin splitting nature of ferromagnetic elements is expected to hinder the emerge of superconductive. The results in Fig. 6 clearly shows a gradual suppression of superconductivity of Re by the incorporation of Co. Superconductivity with T_c beyond liquid helium melting point, 4.2 K, is achieved for ReCo alloys with up to 9% Co, and T_c beyond 2 K with up to 20% Co. By controlling the deposition potential, alloys with different compositions and therefore different superconductivity critical temperatures have been achieved. This provides a future path for pulse deposition of multilayer structures of superconductive and magnetic alloys.

4. Conclusion

Electrodeposition of ReCo alloys is investigated in a water-in-salt electrolyte with 5 M LiCl, where a significantly lowered proton reduction rate is observed. Co electrodeposition starts at a potential of −0.8 V and it is significantly decreased below −1.5 V. LiOH is hypothesized to form, which passivates the electrode surface and/or competes with adsorbed Co intermediate for electrode surface, resulting in the suppression of Co deposition upon the reduction of water. On the other hand, the deposition of Re is promoted. The codeposition of Co not only enhances the deposition of Re at less negative potentials but also inhibits the cathodic stripping of Re into Re^- at more negative potentials.

Significantly different film morphologies and grain structures were observed between the Re, Co, and ReCo alloy films. While the as deposited Re and ReCo alloys are amorphous or nanocrystalline, pure Co is polycrystalline. Polycrystalline HCP crystal structures with significantly grown grains are obtained for Re and ReCo after annealing at 200 °C and a linear relationship between the lattice parameters and alloy composition is observed. A suppression on the superconductivity of Re was observed upon the alloying of Co, resulting in a gradual decrease of critical temperature along the

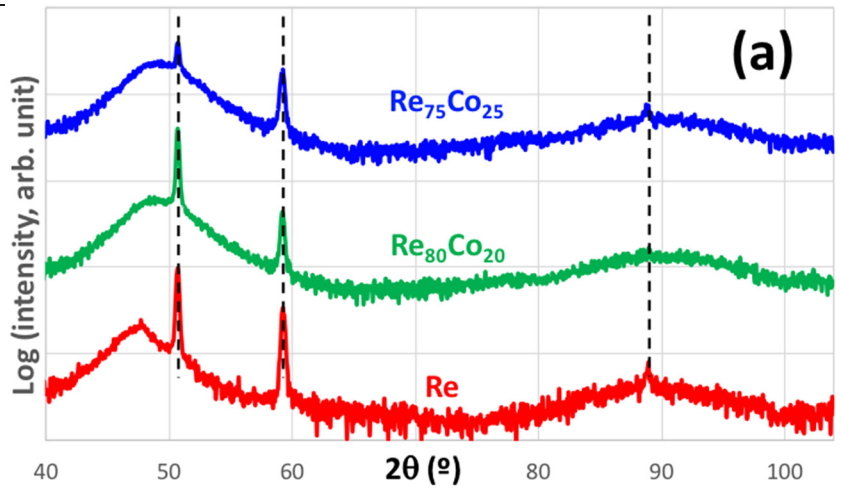

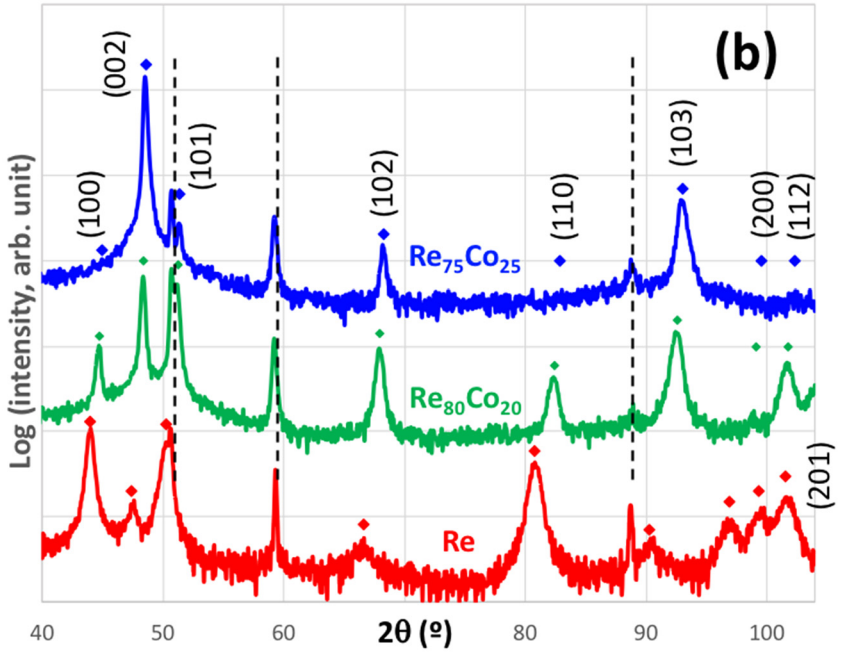

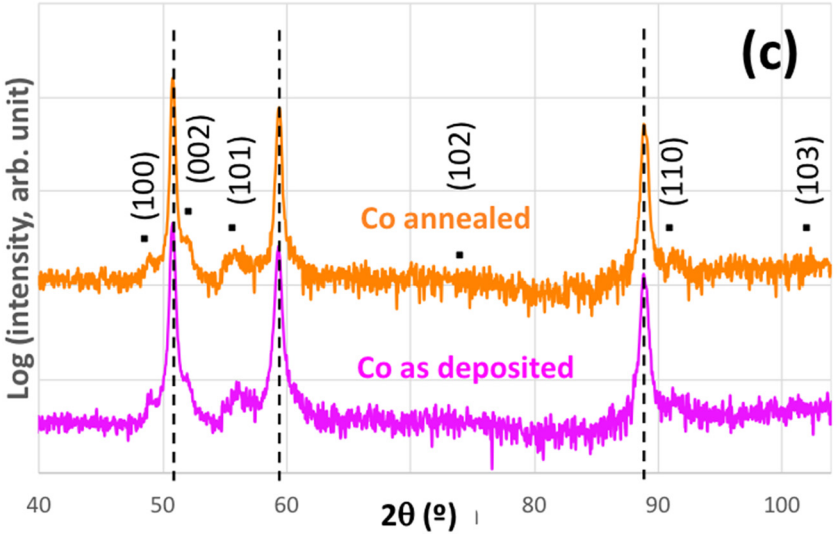

(caption on next page)

Table 3
Lattice parameters of Re and Co from literature and of ReCo from XRD spectrum fitting.

	a (Å)	c (Å)
Re	2.761	4.456
Co	2.5071	4.0965
$Re_{80}Co_{20}$ (−0.8 V)	2.7147	4.3685
$Re_{75}Co_{25}$ (−1.1 V)	2.705	4.3515

Table 4
Full width at half maximum and the estimated grain sizes of electrodeposited Re and ReCo alloy films before and after annealing.

	As deposited			Annealed		
	2 θ	FWHM (°)	Size (nm)	2 θ	FWHM (°)	Size (nm)
Re (100)	47.9	4.05	2.7	43.97	0.4	99.5
$Re_{80}Co_{20}$ (002)	48.7	6.45	1.7	48.3	0.35	202
$Re_{75}Co_{25}$ (002)	49.2	6.65	1.6	49.55	0.35	202

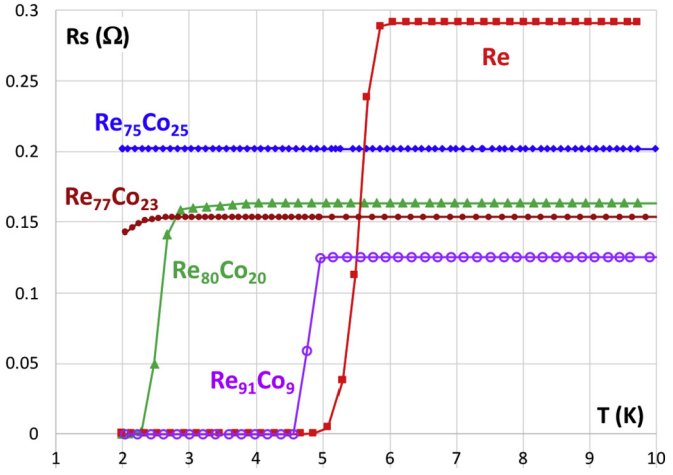

Fig. 6. Resistance of (red) pure Re deposited from Re electrolyte at −1.1 V, (green) $Re_{80}Co_{20}$ and (blue) $Re_{75}Co_{25}$ deposited from ReCo electrolyte at −0.8 and − 1.1 V, respectively, along a temperature sweep from 10 to 2 K. All electrolytes contain 0.1 M H_2SO_4 and 5 M LiCl. Au strips on Si coupons mounted on RDE are used as substrates for deposition. (For interpretation of the references to color in this figure legend, the reader is referred to the web version of this article.)

increase of Co content. A T_c of 4.6 K and 2.3 K is observed for ReCo alloys with 9% and 20% Co, respectively.

Author contribution

QH conceived the experimental idea; SD, WD, TB, and QH conducted experimental plan; SD conducted numerical simulation; WD conducted superconductivity measurements; QH SD prepared and revised the manuscript.

Funding

This research is supported by the National Science Foundation through a grant CMMI-1941820 and the Research Grant Committee at University of Alabama through a grant GR-14741.

Declaration of competing interest

The authors declare that they have no known competing financial interests or personal relationships that could have appeared to influence the work reported in this paper.

Acknowledgement

The Research Grant Council (RGC) at the University of Alabama is acknowledged for support through a grant RG-14741. The National Science Foundation CAREER Program is acknowledged for support through a grant CMMI-1941820. The University of Alabama Central Analytical Facility, Center of Materials for Information Technology Facility, College of Engineering Mechanical Shop, and Chemistry Department Glass Shop are acknowledged for their resources.

Appendix A. Supplementary data

Supplementary data to this article can be found online at https://doi.org/10.1016/j.jelechem.2020.113889.

References

[1] D.P. Pappas, D.E. David, R.E. Lake, M. Bal, R.B. Goldfarb, D.A. Hite, E. Kim, H.-S. Ku, J.L. Long, C.R.H. McRae, L.D. Pappas, A. Roshko, J.G. Wen, B.L.T. Plourde, I. Arslan, X. Wu, Enhanced superconducting transition temperature in electroplated rhenium, Appl. Phys. Lett. 112 (18) (2018), 182601.
[2] J. Daunt, T. Smith, Superconductivity of rhenium, Phys. Rev. 88 (2) (1952) 309.
[3] N. Alekseevskii, M. Mikheeva, N. Tulina, The superconducting properties of rhenium, Soviet Physics JETP 25 (4) (1967).
[4] H. Cao, D. Chai, L. Wu, G. Zheng, Communication—a mechanistic study on electrodeposition of rhenium from acidic solution of ammonium perrhenate, J. Electrochem. Soc. 164 (13) (2017) D825.
[5] C.G. Fink, P. Deren, Rhenium plating, Trans. Electrochem. Soc. 66 (1) (1934) 471.
[6] R. Schrebler, P. Cury, C. Suárez, E. Muñoz, F. Vera, R. Córdova, H. Gómez, J. Ramos-Barrado, D. Leinen, E. Dalchiele, Study of the electrodeposition of rhenium thin films by electrochemical quartz microbalance and X-ray photoelectron spectroscopy, Thin Solid Films 483 (1–2) (2005) 50.
[7] E.C. Muñoz, R.S. Schrebler, M.A. Orellana, R. Córdova, Rhenium electrodeposition process onto p-Si (1 0 0) and electrochemical behaviour of the hydrogen evolution reaction onto p-Si/Re/0.1 M H2SO4 interface, J. Electroanal. Chem. 611 (1–2) (2007) 35.
[8] L. Suo, O. Borodin, T. Gao, M. Olguin, J. Ho, X. Fan, C. Luo, C. Wang, K. Xu, "Water-in-salt" electrolyte enables high-voltage aqueous lithium-ion chemistries, Science 350 (6263) (2015) 938.
[9] L. Coustan, G. Shul, D. Bélanger, Electrochemical behavior of platinum, gold and glassy carbon electrodes in water-in-salt electrolyte, Electrochem. Commun. 77 (2017) 89.
[10] W. Sun, L. Suo, F. Wang, N. Eidson, C. Yang, F. Han, Z. Ma, T. Gao, M. Zhu, C. Wang, "Water-in-Salt" electrolyte enabled LiMn2O4/TiS2 Lithium-ion batteries, Electrochem. Commun. 82 (2017) 71.
[11] L. Suo, O. Borodin, Y. Wang, X. Rong, W. Sun, X. Fan, S. Xu, M.A. Schroeder, A.V. Cresce, F. Wang, "Water-in-salt" electrolyte makes aqueous sodium-ion battery safe, green, and long-lasting, Adv. Energy Mater. 7 (21) (2017), 1701189.
[12] F. Wang, O. Borodin, T. Gao, X. Fan, W. Sun, F. Han, A. Faraone, J.A. Dura, K. Xu, C. Wang, Highly reversible zinc metal anode for aqueous batteries, Nat. Mater. 17 (2018) 543.
[13] Q. Huang, T.W. Lyons, Electrodeposition of rhenium with suppressed hydrogen evolution from water-in-salt electrolyte, Electrochem. Commun. 93 (2018) 53.
[14] Q. Huang, Y. Hu, Electrodeposition of superconducting rhenium with water-in-salt electrolyte, J. Electrochem. Soc. 165 (16) (2018) D796.
[15] T. Kontos, M. Aprili, J. Lesueur, X. Grison, Inhomogeneous superconductivity induced in a ferromagnet by proximity effect, Phys. Rev. Lett. 86 (2) (2001) 304.
[16] T. Kontos, M. Aprili, J. Lesueur, F. Genet, B. Stephanidis, R. Boursier, Josephson junction through a thin ferromagnetic layer: negative coupling, Phys. Rev. Lett. 89 (13) (2002), 137007.
[17] J. Robinson, S. Piano, G. Burnell, C. Bell, M. Blamire, Critical current oscillations in strong ferromagnetic π junctions, Phys. Rev. Lett. 97 (17) (2006) 177003.
[18] T.M.T. Huynh, N.T.M. Hai, P. Broekmann, Quasi-reversible interaction of MPS and chloride on Cu (100) studied by in situ STM, J. Electrochem. Soc. 160 (12) (2013) D3063.
[19] P. Broekmann, M. Wilms, M. Kruft, C. Stuhlmann, K. Wandelt, In-situ STM investigation of specific anion adsorption on Cu (111), J. Electroanal. Chem. 467 (1–2) (1999) 307.

← **Fig. 5.** XRD patterns of (red) pure Re deposited from Re electrolyte at −1.1 V, (green) $Re_{80}Co_{20}$ and (blue) $Re_{75}Co_{25}$ deposited from ReCo electrolyte at −0.8 and − 1.1 V, respectively, (a) before and (b) after annealing at 200 °C; (c) pure Co deposited from Co electrolyte at −1.1 V before and after annealing at 200 °C. All electrolytes contained 0.1 M H_2SO_4 and 5 M LiCl. Cu RDEs are used as substrate for deposition. (For interpretation of the references to color in this figure legend, the reader is referred to the web version of this article.)

[20] W.D. Sides, E. Hassani, D.P. Pappas, Y. Hu, T.S. Oh, Q. Huang, Grain growth and superconductivity of rhenium electrodeposited from water-in-salt electrolytes, J. Appl. Phys. (2019)Submitted for publication.
[21] Y. Marcus, Effect of ions on the structure of water: structure making and breaking, Chem. Rev. 109 (3) (2009) 1346.
[22] Y. Marcus, G. Hefter, Ion pairing, Chem. Rev. 106 (11) (2006) 4585.
[23] H. Du, J.C. Rasaiah, J.D. Miller, Structural and dynamic properties of concentrated alkali halide solutions: a molecular dynamics simulation study, J. Phys. Chem. B 111 (1) (2007) 209.
[24] S. De, J. White, T. Brusuelasa, C. Pattona, A. Koh, Q. Huang, Electrochemical behavior of protons and cupric ions in water in salt electrolytes with alkaline metal chloride, Electrochimica Acta, 2019 Submitted for publication.
[25] N. Dubouis, A. Serva, E. Salager, M. Deschamps, M. Salanne, A. Grimaud, The fate of water at the electrochemical interfaces: electrochemical behavior of free water versus coordinating water, J. Phys. Chem. Lett. 9 (23) (2018) 6683.
[26] K.Y. Sasaki, J.B. Talbot, Electrodeposition of binary iron-group alloys, J. Electrochem. Soc. 142 (3) (1995) 775.
[27] N. Zech, E. Podlaha, D. Landolt, Anomalous codeposition of iron group metals: I. Experimental results, J. Electrochem. Soc. 146 (8) (1999) 2886.
[28] N. Zech, E. Podlaha, D. Landolt, Anomalous codeposition of iron group metals: II. Mathematical model, J. Electrochem. Soc. 146 (8) (1999) 2892.
[29] J.K. Nørskov, T. Bligaard, A. Logadottir, J. Kitchin, J.G. Chen, S. Pandelov, U. Stimming, Trends in the exchange current for hydrogen evolution, J. Electrochem. Soc. 152 (3) (2005) J23.
[30] A. Naor, N. Eliaz, E. Gileadi, Electrodeposition of rhenium–nickel alloys from aqueous solutions, Electrochim. Acta 54 (25) (2009) 6028.
[31] A. Naor, N. Eliaz, L. Burstein, E. Gileadi, Direct experimental support for the catalytic effect of iron-group metals on electrodeposition of rhenium, Electrochem. Solid-State Lett. 13 (12) (2010) D91.
[32] A. Naor, N. Eliaz, E. Gileadi, Electrodeposition of alloys of rhenium with iron-group metals from aqueous solutions, J. Electrochem. Soc. 157 (7) (2010) D422.
[33] T.B. Massalski, H. Okamoto, P. Subramanian, L. Kacprzak, W.W. Scott, Binary Alloy Phase Diagrams, American Society for Metals, Metals Park, OH, 1986.
[34] J. Mallett, W. Shao, D. Liang, G. Zangari, Underpotential codeposition of Cu–Au alloys, Electrochem. Solid-State Lett. 12 (8) (2009) D57.
[35] D. Liang, J.J. Mallett, G. Zangari, Underpotential codeposition of Fe–Pt alloys from an alkaline complexing electrolyte: electrochemical studies, J. Electrochem. Soc. 158 (3) (2011) D149.
[36] K. Mishra, K. Rajeshwar, A voltammetric study of the electrodeposition chemistry in the Cu + In+ Se system, J. Electroanal. Chem. Interfacial Electrochem. 271 (1–2) (1989) 279.
[37] J. Kois, S. Bereznev, E. Mellikov, A. Öpik, Electrodeposition of CuInSe2 thin films onto Mo-glass substrates, Thin Solid Films 511 (2006) 420.
[38] A. Grosse, The isolation of lithium rhenide, Z. Naturforsh. B 8 (10) (1953) 533.
[39] J. Cobble, On the structure of the rhenide ion, J. Phys. Chem. 61 (6) (1957) 727.
[40] A. Woolf, An outline of rhenium chemistry, Q. Rev. Chem. Soc. 15 (3) (1961) 372.
[41] H. Nakano, K. Nakahara, S. Kawano, S. Oue, T. Akiyama, H. Fukushima, Effect of electrolysis factors on crystal orientation and morphology of electrodeposited cobalt, J. Appl. Electrochem. 32 (1) (2002) 43.
[42] M.J. Kim, S. Alvarez, Z. Chen, K.A. Fichthorn, B.J. Wiley, Single-crystal electrochemistry reveals why metal nanowires grow, J. Am. Chem. Soc. 140 (44) (2018), 14740.
[43] E. Gomez, E. Valles, Thick cobalt coatings obtained by electrodeposition, J. Appl. Electrochem. 32 (6) (2002) 693.
[44] M. Winter, WebElements Periodic Table, The University of Sheffield and WebElements Ltd, UK, 1993.